# Coupled Multi-Resolution WMF-FEM to Solve the Forward Problem in Magnetic Induction Tomography Technology

Mohammad Reza Yousefi[1], Farouk Smith[2], Shahrokh Hatefi[2], Khaled Abou-El-Hossein[2], and Jason Z. Kang[3]
[1] Electrical Engineering Department, Najafabad Branch, Islamic Azad University, Najafabad, Iran
[2] Department of Mechatronics, Nelson Mandela University, Port Elizabeth, South Africa
[3] Chengdu College of University Electronic Science and Technology of China, Chengdu, China
Email: mr-yousefi@iaun.ac.ir; {farouk.smith, shahrokh.hatefi, khaled.abou-el-hossein}@mandela.ac.za

***Abstract*—Magnetic Induction Tomography (MIT), is a promising modality used for non-invasive imaging. However, there are some critical limitations in the MIT technique, including the forward problem. In this study, a coupled multi-resolution method combining Wavelet-based Mech Free (WMF) method and Finite Element Method (FEM), short for WMF-FEM method, is proposed to solve the MIT forward problem. Results show that using the WMF-FEM method could successfully solve the mesh coordinates dependence problem in FEM, apply boundary condition in the WMF method, and increase MIT approximations. Simulations show improved results compared to the standard FEM and WFM method. The proposed coupled multi-resolution WMF-FEM method could be used in the MIT technique to solve the forward problem. The contribution of this paper is a simulated MIT system whose performance is closely predicted by mathematical models. The derivation of the simulation equations of the coupled WMF-FEM method is shown. This new approach to the forward problem in MIT has shown an increase in the accuracy in MIT approximations.**

***Index Terms*—Finite element method, magnetic induction tomography, mesh free method, multi-resolution wavelet method**

## I. Introduction

Magnetic Induction Tomography (MIT) is an imaging technique used to measure electromagnetic properties of an object by using the eddy current effect. It is used in industrial processes [1]-[3] as well as medical applications [4]-[13]. The MIT technique is more suitable for non-invasive and non-intrusive applications compared to other tomography solutions, and therefore is considered a safer option. In the MIT technique, a primary magnetic field is generated to induce eddy currents in the object under investigation, by means of an excitation coil. As a result, a secondary magnetic field is produced by these eddy currents and is detected by receiver sensing coils [14]-[17].

By analyzing the difference between the pairs of excitation and sensing coils, the data can be analyzed to reconstruct the cross-sectional image of the object, as well as the spatial distribution of its electrical conductivity. Subsequently, initial estimation of the electrical conductivity and the iterative solution of forward and inverse problems are applied. The forward problem is basically an eddy current problem, in which the electromagnetic field could be described either in terms of a field, an electric potential, or a combination of them [18]-[20]. Analytical solutions for eddy current problems are available only for simple geometries. For more complex geometries, numerical approximations could be implemented. The Finite Element Method (FEM) is a frequently used solution for this purpose [8]. The MIT forward problem is usually solved by using the FEM; which could be described by a classical boundary value problem of a time harmonic eddy current field, which is excited by the primary coils [21]-[24]. In addition, other numerical techniques, for example the Finite Difference (FD) [25], [26] and Boundary Element Method (BEM) [27], have been employed to simulate the MIT measurements and behaviors. In general, the forward problem can be solved by FEM with acceptable accuracy. However, the mesh shape dependence is the major challenge in these methods.

In some electromagnetic tomography applications, the issue becomes worse, when the object volume frequently fluctuates in shape or size. For example, in biomedical applications, large differences can be found in the geometrical properties of a patient's body. In addition, in clinical diagnostics to continuously monitor the human torso, the shape and size of a patient's chest varies periodically with breathing [28], [29]. Moreover, in a FEM model, meshes may affect the uncertainty of the model. Therefore, meshes must be refined in some regions of the solution domain; for example, near a boundary or a sharp edge [30].

On the other hand, when there is a problem with mechanical movements, the Mesh-Free (MF) methods yield better results. The reason is, these methods are based on a set of nodes without using the connectivity of the elements. The Element Free Galerkin (EFG), Mesh Less Local Petrov-Galerkin (MLPG) [31], and Wavelet-based Mesh-Free (WMF) methods [32]-[37] are

Manuscript received January 11, 2020; revised May 30, 2020; accepted July 2, 2020.
Corresponding author: Farouk Smith (email: Farouk.Smith@ mandela.ac.za).

©2020 Int. J. Elec. & Elecn. Eng. & Telcomm.

doi: 10.18178/ijeetc.9.6.380-389

successful and well-known MF solutions. The MLPG approximation relies on defining local shape functions at a set of nodes. The local integrals of shape functions are calculated analytically or numerically in the vicinity of a node. However, in the wavelet-based method, the basis functions are defined over the entire solving domain, and the global integral of the basis functions are calculated on the entire region [32]. Thus, if a set of nodes is displaced by the variation of the object geometries or a mechanical movement, the MLPG and EFG approximation will provide less accurate results compared to the wavelet-based method.

The MF methods are inefficient in applying boundary conditions as they yield a low accuracy in many boundary value problems. Additionally, FEM is an effective method to apply boundary conditions [28], [32]. Therefore, combining these two methods were previously suggested in the literature to solve existing problems [38]-[41]. Furthermore, the combined method was developed and employed for numerical analysis of the electromagnetic fields [42]. The multi-resolution WMF method is more efficient compared to the single scale WMF; due to the ability to select resolution levels in different location of the solution domain [32], [43], [44]. By using multi-resolution analysis, the global stiffness matrix incorporates a high density of zero valued sub-matrices, which would result in a faster inversion procedure [42], [45], [46].

In this paper, a coupled multi-resolution WMF-FEM method is introduced to solve the MIT forward problem. In this study, by using a coupled multi-resolution WMF-FEM method, a new approach is proposed to use essential boundary conditions during an electromagnetic field approximation. A set of simulation results are presented to validate the feasibility of the proposed coupled multi-resolution WMF-FEM method.

## II. Proposed Coupled Multi-Resolution Wavelet-Based Mech Free and Finite Element Method

The proposed system has eight coils that is used for excitation and sensing tasks. The coils have 40-mm inner and 50-mm outer diameters, with a 1mm length. The coils are arranged in a circular ring, which surrounds the object horizontally. The distance between the centers of two coils on opposite sides is 160mm. The region of interest for the imaging is a cylinder with radius of 70 mm (called the conductive volume). In this system, an electrostatic shield was considered around the simulated system. Each coil was excited separately in a predetermined sequence, while the induced voltages in the remaining coils were measured. The excitation current density is 100 A/m$^2$ at a frequency of 5 kHz. In addition, it was assumed that a copper bar with radius of 1.9 mm is inserted in the conductive volume, as a non-magnetic electrically conductive object. Fig. 1 illustrates the coil arrangement and object location in this virtual MIT system, as well as the magnetic permeability and conductivity value in each material.

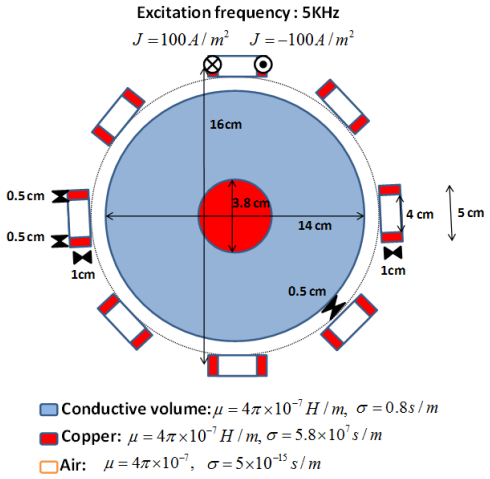


Fig. 1. The arrangement of coils in a simulated MIT system

### A. MIT forward Problem

Image reconstruction in MIT is an inverse problem: the induced voltages in the receiver coils are measured and subsequently, the distribution of the electromagnetic properties of the object would be estimated. In the inverse problem, the experimental data is compared with the simulated voltages in the receiver coils. The data is then simulated in the forward problem by using a given electromagnetic property distribution. The forward problem in MIT is an eddy current problem [47]. It was demonstrated that different formulations would produce the same results in an exact solution and they may differ only in accuracy and computational cost when this solution is implemented.

In general, the forward problem in MIT is governed by Maxwell's equations. If a magnetic vector potential $A$ is assumed constant in the $z$ direction, the conduction current density can be described as [37], [48]:

$$-\nabla\cdot\left[\frac{1}{\mu(x,y)}\nabla A_z(x,y)\right]+j\omega\sigma(x,y)A_z(x,y)=J_s(x,y) \quad (1)$$

where $(x, y)$ represents a point in the two-dimensional (2-D) solution domain $\Omega$. $A_z$ is the magnetic vector potential in the $z$ direction and the source of current is represented by current density $J_s$ of frequency $\omega$. $\sigma$ and $\mu$ are the conductivity and magnetic permittivity, respectively [48]. A weighted combination of Dirichlet and Neumann boundary conditions (Robin boundary condition) is imposed on the boundary of $\Omega$:

$$\frac{1}{\mu(x,y)}\frac{\partial A_z(x,y)}{\partial\hat{n}}\cdot\hat{n}+\gamma A_z(x,y)=q, \text{ on } \partial\Omega \quad (2)$$

where $\partial\Omega$ denotes the boundary enclosing $\Omega$, $\hat{n}$ is the outward normal vector, and $\gamma$ and $q$ are physical parameters of $\partial\Omega$. Moreover, to analyze the measurement data, the induced voltage in the receiver coils could be calculated by mean of Faraday's law of induction:

$$V_{\text{ind}}=-\oint_c E\cdot dl \quad (3)$$

where $c$ is the closed conductive path of a receiver coil.

### B. Coupled WMF-FEM Approach

In the coupled multi-resolution WMF-FEM approach, in order to solve the MIT forward problem, the solution domain is subdivided into two subdomains; a surrounding ($\Omega^{FE}$) and a surrounded ($\Omega^{MF}$) subdomain, which is solved by the FEM and multi-resolution WMF approximation, respectively. As illustrated in Fig. 2, a marginal static subdomain including boundary segments was modeled by FEM, and a central subdomain with a dynamic shape or size was approximated by the multi-resolution WMF method.

#### 1) Finite element method

In the finite element subdomain ($\Omega^{FE}$), to extract the finite element sub-matrices, the Rayleigh-Ritz or Galerkin method could be used. In order to have a coherent solution with the WMF method, the Galerkin method is utilized to formulate the FEM. The Galerkin method is a member of the weighted residuals methods family, which finds the solution by weighting the residual of differential equations. In the Galerkin method, the weighting functions are chosen to be similar to the basis functions [49].

For modeling (1) by FEM, $\Omega^{FE}$ is meshed by triangular elements. The variation of $A_z(x, y)$ in each element is approximated by 2-D linear basis function:

$$A_z^e(x,y) = a_1^e + a_2^e x + a_3^e y \tag{4}$$

Solving the constant coefficients $a_1^e$, $a_2^e$ and $a_3^e$ in element nodes (in terms of potentials) and substituting them in (4) yield

$$A_z^e(x,y) = \sum_{j=1}^{3} N_j^e(x,y) A_j^e \tag{5}$$

where $A_j^e$ and $N_j^e$ are the magnetic vector potential and interpolation function corresponding to node $j$, respectively. Using this model, the weighted residual associated with (1) for element $e$ can be written as [49]

$$\begin{aligned} R_i^e(A_z^e) = \iint_{\Omega^e} \Bigg[ & \frac{1}{\mu^e} \frac{\partial N_i^e(x,y)}{\partial x} \frac{\partial A_z^e(x,y)}{\partial x} + \\ & \frac{1}{\mu^e} \frac{\partial N_i^e(x,y)}{\partial y} \frac{\partial A_z^e(x,y)}{\partial y} + \\ & j\omega\sigma^e N_i^e(x,y) A_z^e(x,y) \Bigg] dxdy - \\ & \iint_{\Omega^e} N_i^e(x,y) J_s^e dxdy - \oint_{\Gamma^e} N_i^e(x,y) D \cdot \hat{n}^e d\Gamma, \\ & \text{for } i = 1,\ 2,\ 3, \text{ and } D = \frac{1}{\mu^e} \nabla A_z^e(x,y) \end{aligned} \tag{6}$$

where $\sigma^e$, $\mu^e$ and $J_s^e$ are constants within the domain of the $e$th element ($\Omega^e$), $\Gamma$ is the boundary of the entire FEM domain and $\Gamma^e$ is the boundary of element $e$. Thus, the sum of all the $\Gamma^e$ is equal to $\Gamma$, and $\hat{n}^e$ is the outward unit vector normal to $\Gamma^e$. This system of equations could be written in matrix form as follow:

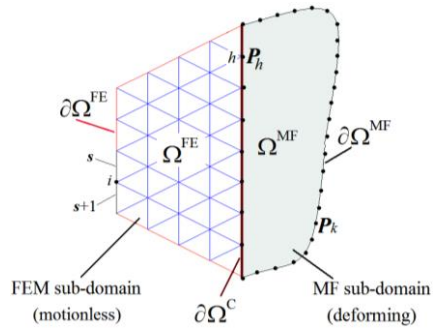


Fig. 2. In the coupled multi-resolution WMF-FEM, a static subdomain is modeled by FEM and a dynamic subdomain is approximated by multi-resolution WMF

$$\left[K^{FE}\right]\left\{A^{FE}\right\} + \left\{g^{FE}\right\} = \left\{F^{FE}\right\} \tag{7}$$

where $K^{FE}$ and $F^{MF}$ are the FEM stiffness and excitation sub-matrices, which are assembled from $\bar{K}^e$ and $\bar{F}^e$, respectively. In addition, $A^{FE}$ denotes the values of $A_z(x,y)$ at the nodes in $\Omega^{FE}$. The elements in $g^{FE}$ have zero value for non-boundary nodes. By applying the homogeneous Neumann or Dirichlet boundary condition, boundary nodes reside on a part of the boundary. The elements for boundary node $i$ residing on a part of the boundary, where the applied Robin boundary condition is defined by [49]

$$g_i = -\int_{\Gamma^s} N_j^e D \cdot \hat{n} d\Gamma - \int_{\Gamma^{s+1}} N_j^e D \cdot \hat{n} d\Gamma \tag{8}$$

where $\Gamma^s$ and $\Gamma^{s+1}$ denote two segments of the boundary of region ($\partial\Omega^{FE}$).

As illustrated in Fig. 2, these two segments are connected to node $I$. The value $i$ is the global node number of the local node $j$ belonging to the element $e$ and $N_j^e$ vanishes at the element side opposite node $j$. This means that $N_j^e$ varies linearly from 1 at node $i$ to 0 at its neighboring nodes. Therefore, by normalizing $\Gamma^s$ and $\Gamma^{s+1}$, (8) could be simplified as follow:

$$g_i = -\int_0^1 \varepsilon D \cdot \hat{n} l^s d\varepsilon - \int_0^1 (1-\varepsilon) D \cdot \hat{n} l^{s+1} d\varepsilon \tag{9}$$

where $l^s$ and $l^{s+1}$ denote the lengths of $\Gamma^s$ and $\Gamma^{s+1}$, respectively. Subsequently, by introducing a Lagrange multiplier for the segment $s$ as follow:

$$\lambda^s = \left[ -\frac{1}{\mu^e} \nabla A_z^e(x,y) \cdot \hat{n} \right] l^s \tag{10}$$

Equation (9) could be transformed to

$$g_i = \int_0^1 \varepsilon \lambda^s d\varepsilon + \int_0^1 (1-\varepsilon) \lambda^{s+1} d\varepsilon \tag{11}$$

The unknown Lagrange multipliers ($\lambda^s$) could be calculated by applying a set of boundary conditions [50], [51]. Assuming that $\lambda^s$ is constant on the segment $s$, following equation could be obtain:

$$g_i = \frac{1}{2}\left(\lambda^s + \lambda^{s+1}\right) \tag{12}$$

Applying this simplification, the system of (7) could be modified to

$$\begin{bmatrix} K^{\mathrm{FE}} & H_v^{\mathrm{FE}} \\ H_u^{\mathrm{FE}} & I^{\mathrm{FE}} \end{bmatrix} \begin{bmatrix} A^{\mathrm{FE}} \\ \lambda^{\mathrm{FE}} \end{bmatrix} = \begin{bmatrix} F^{\mathrm{FE}} \\ q^{\mathrm{FE}} \end{bmatrix} \tag{13}$$

where $H_v^{\mathrm{FE}}$, $H_u^{\mathrm{FE}}$, and $I^{\mathrm{FE}}$ are the sub-matrices used to apply the Robin boundary condition on $\partial\Omega^{\mathrm{FE}}$. According to the simplified equation (12), the $I^{th}$ row of $H_v^{\mathrm{FE}}$ has the value of 1/2 in two positions corresponding to boundary segments $s$ and $s$+1, which are connected to node $i$. Applying the Robin boundary condition and considering a zero value in other positions, we have

$$H_v^{\mathrm{FE}} = \frac{1}{2}\begin{bmatrix} 0 & \cdots & 0 & 0 & 0 & 0 & \cdots & 0 \\ \vdots & \ddots & \vdots & \vdots & \vdots & \vdots & \ddots & \vdots \\ 0 & \cdots & 0 & 0 & 0 & 0 & \cdots & 0 \\ 0 & \cdots & 0 & -1|_{i,s} & -1|_{i,s+1} & 0 & \cdots & 0 \\ 0 & \cdots & 0 & 0 & 0 & 0 & \cdots & 0 \\ \vdots & \ddots & \vdots & \vdots & \vdots & \vdots & \ddots & \vdots \\ 0 & \cdots & 0 & 0 & 0 & 0 & \cdots & 0 \end{bmatrix}_{n\times \mathrm{BS}} \tag{14}$$

where BS is the number of segments of $\partial\Omega^{\mathrm{FE}}$ and $n$ is the number of nodes in $\Omega^{\mathrm{FE}}$. Furthermore, if the boundary condition (2) is assumed for the boundary segments $s$, the $s^{\mathrm{th}}$ row of $H_u^{\mathrm{FE}}$ has the value of $\gamma^s/2$ in the position corresponding to the first node of segment $s$ while considering zero value in other positions. Hence $H_u^{\mathrm{FE}} = (H_v^{\mathrm{FE}})^T$, and we have

$$H_u^{\mathrm{FE}} = \frac{1}{2}\begin{bmatrix} 0 & \cdots & 0 & \gamma^1|_{1,i^1} & 0 & \cdots & 0 \\ 0 & \cdots & 0 & 0 & 0 & \cdots & 0 \\ \vdots & \ddots & \vdots & \vdots & \vdots & \ddots & \vdots \\ 0 & \cdots & 0 & 0 & 0 & \cdots & 0 \\ 0 & \cdots & 0 & \gamma^{\mathrm{BS}}|_{\mathrm{BS},i^{\mathrm{BS}}} & 0 & \cdots & 0 \end{bmatrix}_{\mathrm{BS}\times n} \tag{15}$$

In addition, $I^{\mathrm{FE}}$ is the diagonal matrix whose diagonal elements are $-1/l^s$ ($s$=1, 2, 3, ···, BS):

$$I^{\mathrm{FE}} = \begin{bmatrix} -\frac{1}{l^1} & 0 & \cdots & 0 \\ 0 & -\frac{1}{l^2} & \cdots & 0 \\ \vdots & \vdots & \ddots & \vdots \\ 0 & 0 & \cdots & -\frac{1}{l^{\mathrm{BS}}} \end{bmatrix}_{\mathrm{BS}\times\mathrm{BS}} \tag{16}$$

Also, $q^{\mathrm{FE}}$ is a vector containing boundary condition parameters on the $BS$ boundary segments and $\lambda^{\mathrm{FE}}$ is the corresponding unknown Lagrange multipliers column vector:

$$q^{\mathrm{FE}} = \begin{bmatrix} q^1 & q^2 & \cdots & q^{\mathrm{BS}} \end{bmatrix}^T, \quad \lambda^{\mathrm{FE}} = \begin{bmatrix} \lambda^1 & \lambda^2 & \cdots & \lambda^{\mathrm{BS}} \end{bmatrix}^T \tag{17}$$

Finally, the Dirichlet boundary condition is imposed in $K^{\mathrm{FE}}$ and $F^{\mathrm{FE}}$.

*2) Mesh free method*

The first step in solving the forward problem by using the MF approximation solution is based on the decomposition of an unknown linear function. This function could be decomposed uniquely as linear combinations of linearly independent basis functions [52], as shown below:

$$A_z^{\mathrm{MF}}(x,y) = \sum_{j=1}^{M} c_j \varphi_j(x,y) \tag{18}$$

The unknown coefficients could be estimated by using the Galerkin method of weighted residuals for equation (1); the inner product in this equation with the weight residual function $\phi_i(x, y)$ is given as follows [36]:

$$\begin{aligned} &\underbrace{\iint_{\Omega^{\mathrm{MF}}} -\nabla\cdot\left[\frac{1}{\mu(x,y)}\nabla A_z^{MF}(x,y)\right]\varphi_i(x,y)dxdy}_{\Pi_1} + \\ &\underbrace{\iint_{\Omega^{\mathrm{MF}}} j\omega\sigma(x,y)A_z^{MF}(x,y)\varphi_i(x,y)dxdy}_{\Pi_2} \\ &= \iint_{\Omega^{\mathrm{MF}}} J_s(x,y)\varphi_i(x,y)dxdy \end{aligned} \tag{19}$$

By using the Divergence theorem, $\Pi_1$ could be calculated as follow:

$$\begin{aligned} \Pi_1 = &-\int_{\partial\Omega^{\mathrm{MF}}}\left[\frac{1}{\mu(x,y)}\nabla A_z^{\mathrm{MF}}(x,y)\varphi_i(x,y)\right]\cdot\hat{n}ds + \\ &\iint_{\Omega^{\mathrm{MF}}}\frac{1}{\mu(x,y)}\nabla A_z^{\mathrm{MF}}(x,y)\cdot\nabla\varphi_i(x,y)dxdy \end{aligned} \tag{20}$$

where $ds$ is the element of boundary of MF sub-domain ($\partial\Omega^{\mathrm{MF}}$). If $\partial\Omega^{\mathrm{MF}}$ is partitioned by BP boundary points; by using the left Riemann sum while replacing the combinations of linearly independent basis functions (18) with (20), the following simplified form could be obtained:

$$\begin{aligned} \Pi_1 = &\sum_{k=1}^{\mathrm{BP}-1}\varphi_i(P_k)\lambda^k + \\ &\iint_{\Omega^{\mathrm{MF}}}\frac{1}{\mu(x,y)}\nabla\left(\sum_{j=1}^{M}c_j\varphi_j(x,y)\right)\cdot\nabla\varphi_i(x,y)dxdy \\ \lambda^k = &\left[-\frac{1}{\mu(P_k)}\nabla A_z^{\mathrm{MF}}(P_k)\cdot\hat{n}\right]l^k \end{aligned} \tag{21}$$

where $P_k$ ($k$=1, 2, 3, ···, BP) denotes the coordinate value of the $k^{\mathrm{th}}$ point on $\partial\Omega^{\mathrm{MF}}$ (Fig. 2.), $l^k$ is the distance between $P_k$ and $P_{k+1}$, and $\lambda^k$ is the unknown Lagrange multiplier of segment $k$ [47], [48], [50], [51]. Also, by implementing (18) into $\Pi_2$, the following equation could be obtained:

$$\Pi_2 = \sum_{j=1}^{M} c_j \iint_{\Omega^{\mathrm{MF}}} j\omega\sigma(x,y)\varphi_i(x,y)\varphi_j(x,y)dxdy \tag{22}$$

Substituting (20) and (22) into (19) yields the basis functions (23):

$$\begin{aligned}
&\sum_{j=1}^{M} k_{i,j} c_j + \sum_{k=1}^{\mathrm{BP}-1} \varphi_i(P_k)\lambda_k = F_i \\
&k_{i,j} = \iint_{\Omega^{\mathrm{MF}}} \frac{1}{\mu(x,y)} \nabla\varphi_j(x,y)\cdot\nabla\varphi_i(x,y)dxdy + \\
&\qquad \iint_{\Omega^{\mathrm{MF}}} j\omega\sigma(x,y)\varphi_i(x,y)\varphi_j(x,y)dxdy \\
&F_i = \iint_{\Omega^{\mathrm{MF}}} J_s(x,y)\varphi_i(x,y)dxdy
\end{aligned} \tag{23}$$

where $i$=1, 2, 3, ···, $M$, and $M$ is the number of basis functions. In discrete cases, when the MF sub-domain is discretized to $P\times P$ points, using the first order finite difference method and the left Riemann sum, element $k_{i,j}$ of $K^{\mathrm{MF}}$ and the element $F_i$ of $F^{\mathrm{MF}}$ are specified as follows:

$$\begin{aligned}
k_{i,j} = &\sum_{l=1}^{P-1}\sum_{m=1}^{P-1}\left[\frac{1}{\mu(x_l,y_m)}\frac{\varphi_j(x_l,y_m)-\varphi_j(x_{l-1},y_m)}{\Delta_x}\times\right. \\
&\left.\frac{\varphi_i(x_l,y_m)-\varphi_i(x_{l-1},y_m)}{\Delta_x}\Delta_x\Delta_y\right] + \\
&\sum_{l=1}^{P-1}\sum_{m=1}^{P-1}\left[\frac{1}{\mu(x_l,y_m)}\frac{\varphi_j(x_l,y_m)-\varphi_j(x_l,y_{m-1})}{\Delta_y}\times\right. \\
&\left.\frac{\varphi_i(x_l,y_m)-\varphi_i(x_l,y_{m-1})}{\Delta_y}\Delta_x\Delta_y\right] + \\
&\sum_{l=1}^{P-1}\sum_{m=1}^{P-1} j\omega\sigma(x_l,y_m)\varphi_j(x_l,y_m)\varphi_i(x_l,y_m)\Delta_x\Delta_y \\
F_i = &\sum_{l=1}^{P-1}\sum_{m=1}^{P-1} J_s(x_l,y_m)\varphi_i(x_l,y_m)\Delta_x\Delta_y
\end{aligned} \tag{24}$$

$$\begin{aligned}
H_v^{\mathrm{MF}} &= \begin{bmatrix} \varphi_1(P_1) & \cdots & \varphi_1(P_{\mathrm{BP}-1}) \\ \vdots & \ddots & \vdots \\ \varphi_M(P_1) & \cdots & \varphi_M(P_{\mathrm{BP}-1}) \end{bmatrix}_{M\times(\mathrm{BP}-1)} \\
H_u^{\mathrm{MF}} &= \begin{bmatrix} \gamma^1\varphi_1(P_1)+\frac{1}{\mu_1}\frac{\partial\varphi_1}{\partial\hat{n}}\cdot\hat{n}\Big]_{P_1} & \cdots & \gamma^1\varphi_M(P_1)+\frac{1}{\mu_1}\frac{\partial\varphi_M}{\partial\hat{n}}\cdot\hat{n}\Big]_{P_1} \\ \vdots & \ddots & \vdots \\ \gamma^{\mathrm{BP}-1}\varphi_1(P_{\mathrm{BP}-1})+\frac{1}{\mu_{\mathrm{BP}-1}}\frac{\partial\varphi_1}{\partial\hat{n}}\cdot\hat{n}\Big]_{P_{\mathrm{BP}-1}} & \cdots & \gamma^{BP-1}\varphi_M(P_{\mathrm{BP}-1})+\frac{1}{\mu_{\mathrm{BP}-1}}\frac{\partial\varphi_M}{\partial\hat{n}}\cdot\hat{n}\Big]_{P_{\mathrm{BP}-1}} \end{bmatrix}_{M\times(\mathrm{BP}-1)} \\
q^{\mathrm{MF}} &= \begin{bmatrix} q^1 & q^2 & \cdots & q^{\mathrm{BP}-1} \end{bmatrix}^T
\end{aligned} \tag{25}$$

$H_v^{\mathrm{MF}}$, $H_u^{\mathrm{MF}}$, and $q^{\mathrm{MF}}$ are used for applying the boundary conditions (2) for BP boundary segments, which could be defined as (25).

Finally, the unknown coefficients $\vartheta^{\mathrm{MF}}$ and Lagrange multipliers $\lambda^{\mathrm{MF}}$ could be calculated as follows:

$$\vartheta^{\mathrm{MF}} = \begin{bmatrix} c_1 & \cdots & c_M \end{bmatrix}^T,\ \lambda^{\mathrm{MF}} = \begin{bmatrix} \lambda^1 & \cdots & \lambda^{\mathrm{BP}-1} \end{bmatrix}^T \tag{26}$$

*3) Coupled WMF-FEM*

In the coupled WMF-FEM, a surrounding static subdomain is modeled by FEM and a surrounded dynamic subdomain is approximated by WMF. Therefore, FEM applies the boundary conditions to the surrounding static subdomain effectively. On the other hand, WMF alleviates errors caused by changing the object shape or size in the surrounded subdomain (Fig. 2). Furthermore, in both WMF and FEM sub-domains, the magnetic vector potential and its gradient (defined as Lagrange multiplier) should be similar (continuity conditions) at each node on the boundary between the two regions ($\partial\Omega^C$):

$$\begin{aligned}
&A_z^{\mathrm{MF}}(x_h,y_h) = A_z^{\mathrm{FE}}(x_h,y_h) \\
&\lambda^h = -\lambda^S = \lambda^k
\end{aligned} \tag{27}$$

where $A_z^{\mathrm{MF}}$ and $A_z^{\mathrm{FE}}$ are the magnetic vector potentials in WMF and FEM subdomains, respectively. $\lambda^h$ is the $h^{\mathrm{th}}$ Lagrange multiplier corresponding to the common boundary node $P_h(x_h,y_h)$ on $\partial\Omega^C$, $k$ is the WMF boundary point associated with node $h$, and $s$ is the FEM boundary segment connected to node $h$ (Fig. 2). Finally, the global equation could be written in the matrix form as follows [28]:

$$\begin{bmatrix} K^{\mathrm{FE}} & 0 & H_v^{\mathrm{FE}} & 0 & G_v^{\mathrm{FE}} \\ 0 & K^{\mathrm{MF}} & 0 & H_v^{\mathrm{MF}} & G_v^{\mathrm{MF}} \\ H_u^{\mathrm{FE}} & 0 & I^{\mathrm{FE}} & 0 & 0 \\ 0 & H_u^{\mathrm{MF}} & 0 & 0 & 0 \\ G_u^{\mathrm{MF}} & G_u^{\mathrm{MF}} & 0 & 0 & 0 \end{bmatrix} \begin{bmatrix} A^{\mathrm{FE}} \\ \vartheta^{\mathrm{MF}} \\ \lambda^{\mathrm{FE}} \\ \lambda^{\mathrm{MF}} \\ \lambda^c \end{bmatrix} = \begin{bmatrix} F^{\mathrm{FE}} \\ F^{\mathrm{MF}} \\ q^{\mathrm{FE}} \\ q^{\mathrm{MF}} \\ 0 \end{bmatrix} \tag{28}$$

By using $G_v^{\mathrm{FE}}$, $G_u^{\mathrm{FE}}$, $G_v^{\mathrm{MF}}$, $G_u^{\mathrm{MF}}$, and $\lambda^c$ the continuity conditions on $\partial\Omega^C$ could be reinforced [36]. By replacing (18) into conditions (27), following sub-matrices could be determined as

$$\begin{aligned}
G_u^{\mathrm{FE}} &= \left(G_v^{\mathrm{FE}}\right)^T = \begin{bmatrix} 0 & \cdots & -1\big|_{1,i^1} & \cdots & 0 \\ \vdots & \vdots & \ddots & \vdots & \vdots \\ 0 & \cdots & -1\big|_{\mathrm{nc},i^{\mathrm{nc}}} & \cdots & 0 \end{bmatrix}_{\mathrm{nc}\times n} \\
G_u^{\mathrm{MF}} &= \left(G_v^{\mathrm{MF}}\right)^T = \begin{bmatrix} \varphi_1(P_1) & \cdots & \varphi_M(P_1) \\ \vdots & \ddots & \vdots \\ \varphi_1(P_{\mathrm{nc}}) & \cdots & \varphi_M(P_{\mathrm{nc}}) \end{bmatrix}_{\mathrm{nc}\times M} \\
\lambda^c &= \begin{bmatrix} \lambda^1 & \lambda^2 & \cdots & \lambda^{\mathrm{nc}} \end{bmatrix}^T
\end{aligned} \tag{29}$$

where nc is the number of common boundary nodes on $\partial\Omega^C$, $n$ is the number of nodes in $\Omega^{\mathrm{FE}}$, and $M$ is the number of basic functions in $\Omega^{\mathrm{MF}}$.

It should be mentioned that the proposed method has high flexibility in terms of the stiffness matrix. The reason for that is that the $\Omega^{FE}$ and $\Omega^{MF}$ sub-domains are represented by two separate partitions in the global stiffness matrix. Therefore, by varying the geometry of sub-domain $\Omega^{M}$, only the MF sub-matrix needs to be updated [28].

*4) Multi-resolution wavelet basis functions*

To represent the multi-resolution WMF basis set, the basic wavelet functions are used in different scales. To extract the details of approximation in last level, a scaling function is used to estimate the average value of the unknown function. The scaling function has a nonzero mean, which is appropriate to extract approximation details. On the other hand, the boundary conditions were successfully applied by introducing the boundary and interface jump functions into the set of basis functions. Therefore, by using a specific procedure [38], the 2-D multi-resolution WMF basis set is represented by

$$A_z^{MF}(x,y) = \sum_{j,i_1,i_2,l} d^l_{j,i_1,i_2}\psi^l_{j,i_1,i_2}(x,y) + \sum_{i_1,i_2} a_{i_1,i_2}\phi^J_{i_1,i_2}(x,y) + \sum_{k,r} b^r_k \varphi^r_k(x,y) \quad (30)$$

$$\text{for } l = 1,\ 2,\ 3;\quad r = 1,\ 2,\ 3,\ 4$$

where $d^l_{j,i_1,i_2}$ and $a_{i_1,i_2}$ are unknown details and approximation coefficients, and $b^r_k$ is an unknown boundary and interface coefficient. $\psi^l_{j,i_1,i_2}$ represents the 2-D basic wavelet function obtained by scaling $\psi^l(x)$ with a binary scaling factor ($j$) and translating it with dyadic translation factors $i_1$ and $i_2$. ( $-\infty < i_1,\ i_2 < \infty$ ), $\phi^J_{i_1,i_2}$ are 2-D corresponding scaling functions in the last level, and ($J$) and $\varphi^r_k(x)$ are the 2-D slope jump functions; for the $k^{th}$ rectangle part of the MF sub-domain. In each vertex, one jump function (boundary or interface) is required for enforcing the boundary and interface conditions [38].

## III. Results and Discussion

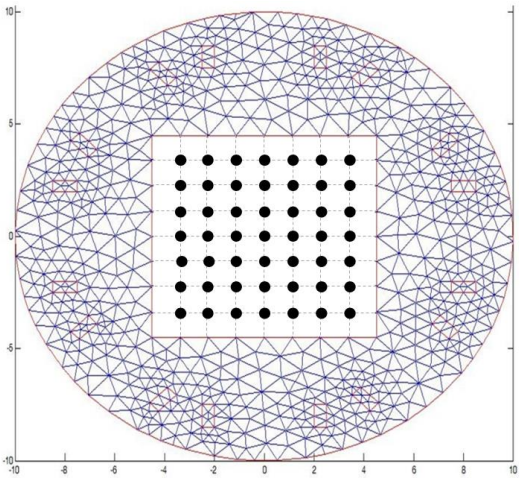

Fig. 3. Meshing the marginal sub-domain for solving by FEM in the proposed approach. The central sub-domain is considered for solving by MF method. Dashed lines shown placement of the used jump functions in MF subdomain.

In the simulated MIT system, using MATLAB/ SIMULINK software, the proposed coupled multi-resolution WMF-FEM was used to solve the MIT forward problem. In Fig. 1, the MF sub-domain with dimension of 80mm×80mm was considered to solve the problem by multi-resolution WMF inside the conductive volume. This sub-domain is netted into 81×81 points and 192 third order Daubechies (db3) wavelet basis, 64 related scaling (1 scaling function in each sub-region) and 81 slope jump functions (1 jump function on each vertex) constitute the orthogonal basis set, where, these coefficients are unknown. Furthermore, the surrounding sub-domain was meshed into 1439 triangular elements (using 763 nodes), as illustrated in Fig. 3.

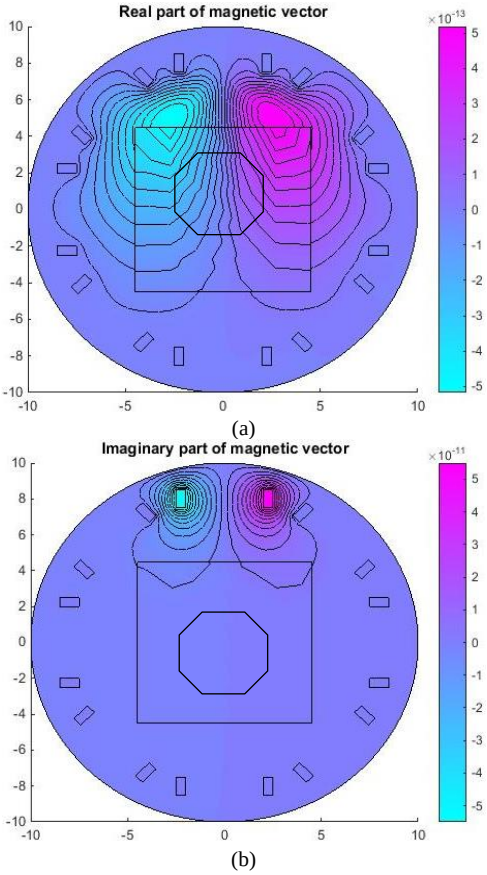


(a)

(b)

Fig. 4. (a) Real and (b) imaginary distribution of the magnetic vector potential in the simulated MIT system, obtained from the proposed WMF-FEM method

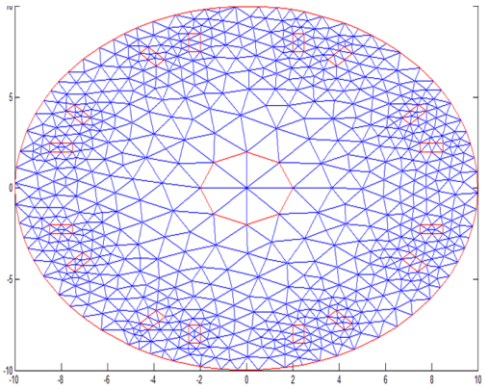

Fig. 5. Meshing the total solving domain of the simulated MIT system for employment by standard FEM.

Afterwards, the coupled multi-resolution WMF-FEM was applied to solve (3). The distribution of the real and imaginary part of the resulting magnetic vector potential is shown in Fig. 4.

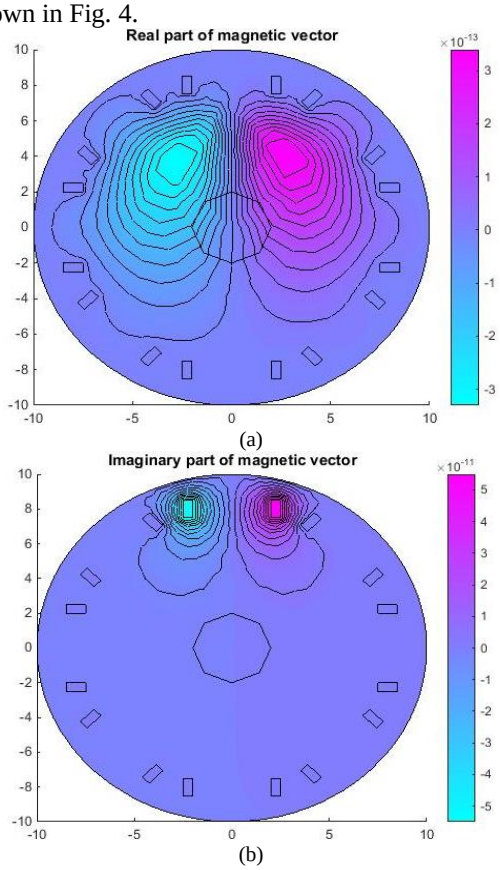


(a)

(b)

Fig. 6. (a) Real and (b) imaginary distribution of magnetic vector potential in standard FEM.

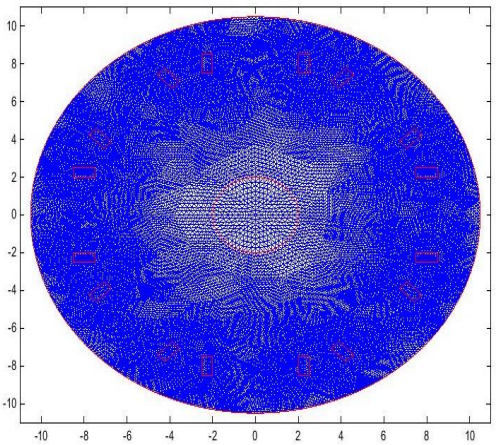

Fig. 7. Structure of refined mesh employed in exact solution.

On the other hand, to illustrate the effectiveness of coupled multi-resolution WMF-FEM, by using 765 nodes, the simulated system is meshed into 1443 triangular elements (as shown in Fig. 5) and solved by standard FEM. Fig. 6 illustrates the distribution of the real magnetic vector potential which is obtained from the standard FEM. In order to compare the effectiveness of these two different solutions, the proposed coupled multi-resolution WMF-FEM and standard FEM, the exact solution is calculated by the refined FEM (mesh includes 47181 nodes and 93760 elements), as shown in Fig. 7 (refined mesh is used). Fig. 8 illustrate the real and imaginary part of the accurate answer extracted from the refined mesh (Fig. 7) for the performance comparison of the proposed method and the standard FEM.

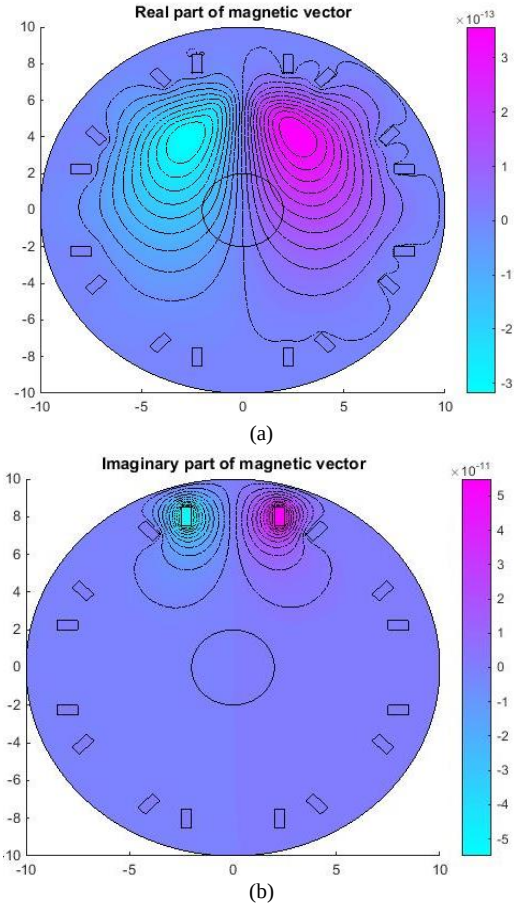


(a)

(b)

Fig. 8. (a) Real and (b) imaginary distribution of exact solution (Refined FEM)

To compare the standard FE with the proposed solution, the following norm error rate criteria was used:

$$\%\text{error}_{\text{rmsn}} = 100 \times \frac{\sqrt{\sum_{i=1}^{N} (A_i - \tilde{A}_i)^2}}{\sqrt{\sum_{i=1}^{N} \tilde{A}_i^2}} \tag{31}$$

where $A_i$ and $\tilde{A}_i$ are the exact and approximated values at each point, respectively.

TABLE I: COMPARISON OF THE PROPOSED COUPLED MULTI-RESOLUTION WMF-FEM AND STANDARD FEM IN MAGNITUDE NORM ERROR

| Norm error rate in magnitude | MF sub-domain | FEM sub-domain | Entire solution domain |
|---|---|---|---|
| Standard FEM compared to exact solution | 7.065% | 3.531% | 3.538% |
| Proposed method compared to exact solution | 4.473% | 3.276% | 3.278% |

The results were obtained by using a Core i7 3.06 GHz CPU, 4 GB RAM workstation. The norm error rate in magnitude is given in Table I. The corresponding error in signal phase is given in Table II. In addition, the performance of the proposed coupled multi-resolution WMF-FEM, coupled WMF-FEM [37], and standard FEM is compared in Table III. Simulation results have demonstrated that the proposed multi-resolution WMF-FEM could improve the accuracy of approximations. Therefore, the degree of freedom in WMF-FEM is more than the standard FEM. Increasing the number of jump functions in the common boundary of the two WMF and FEM regions leads to an increased degree of freedom, as well as mean relative error rate reduction, especially on the common boundary. However, by using the proposed solution, computational cost and CPU time factors would increase when the accuracy of the system is increased. Better performances may be achieved by performing optimization between accuracy and CPU time, as well as selecting the FEM and WMF sub-domains, and optimizing of wavelet scales. The combined multi-resolution WMF and FEM has advantages of solving the mesh coordinates dependence problem in the FEM, and applying boundary condition and computational cost constraints in the WMF method.

TABLE II: COMPARISON OF THE PROPOSED COUPLED MULTI-RESOLUTION WMF-FEM AND STANDARD FEM IN PHASE ERROR

| Error in phase | MF sub-domain | FEM sub-domain | Entire solution domain |
|---|---|---|---|
| Standard FEM compared to exact solution | 0.029% | 0.282% | 0.271% |
| Proposed method compared to exact solution | 0.086% | 0.286% | 0.276% |

TABLE III: PERFORMANCE COMPARISON OF THE PROPOSED MULTI-RESOLUTION COUPLED WMF-FEM AND STANDARD FEM IN NORM ERROR RATE AND CALCULATION TIME IN DIFFERENT CASES

| Method | No. FEM nodes | No. basis functions | | | | Total DOFs | Norm error | CPU (s) |
|---|---|---|---|---|---|---|---|---|
| | | Wavelet functions | Scaling functions | Jump functions | Total | | | |
| Refined FEM | 47181 | - | - | - | - | 47181 | Reference | 3.09 |
| Standard FEM | 765 | - | - | - | - | 765 | 3.538% | 0.72 |
| Coupled WMF-FEM (single resolution) [37] | 760 | - | 1225 | 81 | 1306 | 2066 | 3.388% | 3.59 |
| Proposed coupled multi-resolution WMF-FEM (initial mesh & nodes) | 763 | 192 | 64 | 9 | 265 | 1028 | 4.437% | 0.47 |
| | 763 | 192 | 64 | 25 | 281 | 1044 | 3.273% | 0.55 |
| | 763 | 192 | 64 | 81 | 337 | 1100 | 3.273% | 0.67 |
| Proposed coupled multi-resolution WMF-FEM (refined mesh & nodes) | 2835 | 768 | 256 | 289 | 1313 | 4148 | 1.455% | 9.51 |

## IV. CONCLUSIONS

The purpose of this paper was to introduce a coupled multi-resolution WMF and FEM method to solve the MIT forward problem.

The methodology was to use a coupled multi-resolution WMF and FEM, a new approach to use essential boundary conditions during an electromagnetic field approximation. The forward problem was formulated using three mathematical models of the system. It was solved using the finite element method, the mesh free method, and using a combination of Wavelet-based Mesh-Free and Finite Element methods.

The last combination of using WMF and FEM, reduced computational costs and solved the mesh coordinates dependence problem in the Finite Element technique. The technical advantages and constrains of the proposed method were compared to the standard FEM, in terms of accuracy and CPU time. Although, the improvement in accuracy is compromised with increased computational cost, the results have shown that the proposed method improved the accuracy of approximations.

This originality and contribution that this paper demonstrated was a simulated MIT system whose performance was closely predicted by mathematical models. The derivation of the simulation equations of the coupled Wavelet-based Mesh-Free and Finite Element methods was shown. This new approach to the forward problem in MIT has shown an increase in the accuracy in MIT approximations.

## CONFLICT OF INTEREST

The authors declare no conflict of interest.

## AUTHOR CONTRIBUTIONS

Mohammad Reza Yousefi and Shahrokh Hatefi researched the literature, conceived the study, and performed the product design and testing, and wrote the original draft of the manuscript. Farouk Smith checked and verified the mathematical development, language editing, contributed to the research plan and manuscript preparation. Khaled Abou-El-Hossein contributed to the research plan and manuscript preparation. Jason Z. Kang suggested remarks for enhancing the integrity of the paper. All authors read and approved the final version.

## REFERENCES

[1] M. Lu and M. Soleimani, "Magnetic induction tomography methods and applications: A review," *Measurement Science and Technology*, vol. 28, no. 7, p. 072001, 2017.

[2] J. Yao and M. Takei, "Application of process tomography to multiphase flow measurement in industrial and biomedical fields: A review," *IEEE Sensors Journal*, vol. 17, no. 24, pp. 8196-8205, 2017.

[3] C. Tan, J. Jia, C. Xu, and Z. Sun, "IEEE access special section Editorial: Multiphase flow measurement: Techniques and applications," *IEEE Access*, vol. 6, pp. 32673-32675, June 2018.

[4] L. Ma and M Soleimani, "Magnetic induction tomography methods and applications: A review," *Measurement Science and Technology*, vol. 28, no. 7, p. 072001, June 2017.

[5] Z. Xiao, C. Tan, and F Dong, "3-D hemorrhage imaging by cambered magnetic induction tomography," *IEEE Trans. on Instrumentation and Measurement*, vol. 68, no. 7, pp. 2460-2468, 2019.

[6] C. Bathke, T. Kluth, C. Brandt, and P. Maaß, "Improved image reconstruction in magnetic particle imaging using structural a priori information," *International Journal on Magnetic Particle Imaging*, vol. 3, no. 1, Mar. 2017.

[7] L. Wang, "Electromagnetic induction holography imaging for stroke detection," *JOSA A*, vol. 34, no. 2, pp. 294-298, 2017.

[8] J. Jeon, W. Chung, and H. Son, "Magnetic induction tomography using magnetic dipole and lumped parameter model," *IEEE Access*, vol. 7, pp. 70287-70295, May 2019.

[9] M. Klein, D. Erni, and D. Rueter, "Three-dimensional magnetic induction tomography: Improved performance for the center regions inside a low conductive and voluminous body," *Sensors*, vol. 20, no. 5, p. 1306, 2020.

[10] L. Vasung, E. A. Turk, S. L. Ferradal, *et al.*, "Exploring early human brain development with structural and physiological neuroimaging," *NeuroImage*, vol. 187, pp. 226-254, Feb. 2019.

[11] M. J. Cha, H. J. Park, M. Y. Paek, *et al.*, "Free-breathing ultrashort echo time lung magnetic resonance imaging using stack-of-spirals acquisition: A feasibility study in oncology patients," *Magnetic Resonance Imaging*, vol. 51, pp. 137-143, Sept. 2018.

[12] H. Ammari, L. Qiu, F. Santosa, and W. Zhang, "Determining anisotropic conductivity using diffusion tensor imaging data in magneto-acoustic tomography with magnetic induction," *Inverse Problems*, vol. 33, no. 12, 2017.

[13] Z. Su, S. Ventre, L. Udpa, and A. Tamburrino, "Monotonicity based imaging method for time-domain eddy current problems," *Inverse Problems*, vol. 33, no. 12, 2017.

[14] J. Jeon, W. Chung, and H. Son, "Magnetic induction tomography using magnetic dipole and lumped parameter model," *IEEE Access*, vol. 7, pp. 70287-70295, May 2019.

[15] J. Xiang, Y. Dong, M. Zhang, and Y. Li, "Design of a magnetic induction tomography system by gradiometer coils for conductive fluid imaging," *IEEE Access*, vol. 7, pp. 56733-56744, May 2019.

[16] M. Soleimani, W. R. B. Lionheart, A. J. Peyton, X. Ma, and S. R. Higson, "A three-dimensional inverse finite element method applied to experimental eddy current imaging data," *IEEE Trans. Magn.*, vol. 42, no. 5, pp. 1560-1567, 2006.

[17] Y. Arellano, L. Ma, A. Hunt, and O. Haas, "Characterisation of the effects of sensor geometry on the performance of magnetic induction tomography systems," in *Proc. 9th World Conference on Industrial Process Tomography, International Society for Industrial Process Tomography*, 2019, pp. 373-382.

[18] K. Stawicki, B. Szuflitowska, and M. Ziolkowski, "Recent simulation results of the magnetic induction tomography forward problem," *Archives of Electrical Engineering*, vol. 65, no. 2, pp. 327-336, 2016.

[19] D. Yang, Y. Liu, B. Xu, and J. Pang, "Simulation study for forward problem in magnetic induction tomography by COMSOL," in *Proc. Chinese Control and Decision Conference*, 2019, pp. 124-129.

[20] E. C. Morales, C. D. Acosta-Medina, G. Castellanos-Dominguez, and D. Mantini, "A finite-difference solution for the EEG forward problem in inhomogeneous anisotropic media," *Brain Topography*, vol. 32, no. 2, pp. 229-239, 2019.

[21] L. Ma and M. Soleimani, "Magnetic induction tomography methods and applications: A review," *Measurement Science and Technology*, vol. 28, no. 7, 2017.

[22] B. Hao, K. M. Lee, and K. Bai, "Distributed current source modeling method for 3D eddy current problem in magnetic conductor with discrete state-space *J-φ* formulation." *Journal of Computational Physics*, vol. 401, Jan. 2020.

[23] L. Ke, W. Zu, Q. Du, J. Chen, and X. Ding, "A bio-impedance quantitative method based on magnetic induction tomography for intracranial hematoma," *Medical & Biological Engineering & Computing*, vol. 58, no. 857-869, Feb. 2020.

[24] L. Ma, R. Banasiak, and M. Soleimani, "Magnetic induction tomography with high performance GPU implementation," *Progress in Electromagnetics Research*, vol. 65, pp. 49-63, 2016.

[25] M. Ziolkowski, S. Gratkowski, and A. R. Zywica, "Analytical and numerical models of the magnetoacoustic tomography with magnetic induction," *The International Journal for Computation and Mathematics in Electrical and Electronic Engineering*, vol. 37, no. 2, pp. 538-548, 2018.

[26] Y. Chen, Q. Chen, J. Sun, L. Zhang, and L. Tan, "Multimodal monitoring technologies for pathophysiology and management of traumatic brain injury," *Journal of Translational Critical Care Medicine*, vol. 1, no. 1, p. 12, 2019.

[27] P. D. Tillieux and Y. Goussard, "A volumetric integral equation formulation for magnetic induction tomography," in *Proc. IEEE Conference on Antenna Measurements & Applications*, 2016, pp. 1-4.

[28] L. A. Bueno, E. A. Divo, and A. J. Kassab. "Multi-scale cardiovascular flow analysis by an integrated meshless-lumped parameter model," *International Journal of Computational Methods and Experimental Measurements*, vol. 6, no. 6, pp. 1138-1148, Jan 2018.

[29] B. Sun, S. Yue, Z. Hao, Z. Cui, and H. Wang, "An improved Tikhonov regularization method for lung cancer monitoring using electrical impedance tomography," *IEEE Sensors Journal*, vol. 19, no. 8, pp. 3049-3057, 2019.

[30] R. Huang and L. Mu. "A new fast method of solving the high dimensional elliptic eigenvalue problem," *Applied Mathematics and Computation*, vol. 356, pp. 338-346, Sept. 2019.

[31] B. Tang, S. Li, and X. Cui, "A gradient weighted finite element method (GW-FEM) for static and quasi-static electromagnetic field computation," *International Journal of Computational Methods*, vol. 17, no. 6, 2020.

[32] B. Nagevadiya, B. Vaghasia, N. Rachchh, and R. Bhroniya, "Galerkin meshfree methods: A review and mathematical implementation aspects," *International Journal of Applied and Computational Mathematics*, vol. 5, no. 4, p. 105, 2019.

[33] F. Bulut, "An alternative approach to compute wavelet connection coefficients," *Applied Mathematics Letters*, vol. 53, pp. 1-9, Mar. 2016.

[34] S. Amat, P. J. Blazquez, S. Busquier, and C. Bermudez, "Wavelets for the Maxwell's equations: An overview," *Journal of Computational and Applied Mathematics*, vol. 321, pp. 555-565, Sept. 2017.

[35] M. R. Yousefi, R. Jafari, and H. Abrishami-Moghaddam, "A combined wavelet-based mesh-free method for solving the forward problem in electrical impedance tomography," in *Proc. IEEE Int. Symp. Med. Meas. Appl. Proc.*, 2012, pp. 251-254.

[36] M. R. Yousefi, R. Jafari, and H. Abrishami-Moghaddam, "A combined wavelet-based mesh-free method for solving the forward problem in electrical impedance tomography," *IEEE Trans. Instrum. Meas.*, vol. 62, no. 10, pp. 2629-2638, 2013.

[37] M. R. Yousefi, R. Jafari, and H. A. Moghaddam, "A combined wavelet based mesh free-finite element method for solving the forward problem in magnetic induction tomography," *Iranian J. Biomed. Eng.*, vol. 8, no. 1, pp. 69-86, 2014.

[38] Y. Zhang, W. Ge, Y. Zhang, and Z. Zhao, "Topology optimization method with direct coupled finite element–element-free Galerkin method," *Advances in Engineering Software*, vol. 115, pp. 217-229, Jan. 2018.

[39] A. Shojaei, T. Mudric, M. Zaccariotto, and U. Galvanetto, "A coupled meshless finite point/peridynamic method for 2D dynamic fracture analysis," *International Journal of Mechanical Sciences*, vol. 119, pp. 419-431, Dec. 2016.

[40] M. Li, X. D. Ye, F. Xu, and Y. T. Yang, "An iterative CN-leapfrog scheme based hybrid implicit–explicit discontinuous Galerkin finite-element time-domain method for analysis of multiscale problems," *Applied Computational Electromagnetics Society Journal*, vol. 33, no. 6, pp. 597-602, 2018.

[41] Z. Y. Li, Z. J. Chen, X. H. Wu, and W. Q. Tao, "Coupled MLPG–FVM simulation of steady state heat conduction in irregular geometry." *Engineering Analysis with Boundary Elements*, vol. 100, pp. 265-275, Mar. 2019.

[42] M. R. Yousefi, R. Jafari, and H. A. Moghaddam, "Imposing boundary and interface conditions in multi-resolution wavelet Galerkin method for numerical solution of Helmholtz problems," *Computer Methods Appl. Mech. Eng.*, vol. 276, pp. 67-94, Jul. 2014.

[43] P. C. L. D. Silva, J. P. D. Silva, and A. R. G. Garcia, "Daubechies wavelets as basis functions for the vectorial beam propagation method," *Journal of Electromagnetic Waves and Applications*, vol. 33, no. 8, pp. 1027-1041, 2019.

[44] N. Hussain, M. N. Karsiti, N. Yahya, and V. Jeoti, "2D wavelets Galerkin method for the computation of EM field on seafloor excited by a point source," *International Journal of Applied Electromagnetics and Mechanics*, vol. 53, no.4, pp. 631-644, 2017.

[45] V. H. Ferreira, R. Zanghi, M. Z. Fortes, *et al*., "A survey on intelligent system application to fault diagnosis in electric power system transmission lines," *Electric Power Systems Research*, vol. 136, pp. 135-153, Jul. 2016.

[46] M. A. Joshi, "Digital image processing: An algorithmic approach," *PHI Learning Pvt. Ltd.*, 2018.

[47] B. Dekdouk, C. Ktistis, D. W. Armitage, and A. J. Peyton, "Absolute imaging of low conductivity material distributions using nonlinear reconstruction methods in magnetic induction tomography," *Progress in Electromagnetics Research*, vol. 155, pp. 1-18, Jan. 2016.

[48] L. Ke, L. Yin, Q. Du, and W. Zu, "Study on back projection iteration reconstruction method based on sensitivity matrix for magnetic induction tomography," in *Proc. Third International Conference on Biological Information and Biomedical Engineering*, 2019, pp. 1-5.

[49] J. M. Jin, *The Finite Element Method in Electromagnetics*, John Wiley & Sons, 2015.

[50] G. R. Joldes, H. Chowdhury, A. Wittek, and K. Miller, "A new method for essential boundary conditions imposition in explicit meshless methods," *Engineering Analysis with Boundary Elements*, vol. 80, pp. 94-104, Jul. 2017.

[51] S. Mehraeen and J. S. Chen, "Wavelet Galerkin method in multi-scale homogenization of heterogeneous media," *Int. J. Numer. Methods Eng.*, vol. 66, no. 3, pp. 381-403, 2006.

[52] M. N. O. Sadiku, *Numerical Techniques in Electromagnetics with MATLAB*, CRC Press, 2018.

Copyright © 2020 by the authors. This is an open access article distributed under the Creative Commons Attribution License (CC BY-NC-ND 4.0), which permits use, distribution and reproduction in any medium, provided that the article is properly cited, the use is non-commercial and no modifications or adaptations are made.

**Mohammad Reza Yousefi** received the B.Sc. degree in electrical engineering from Islamic Azad University, Najafabad Branch, Isfahan, Iran, and the M.Sc. and Ph.D. degrees in biomedical engineering from the K. N. Toosi University of Technology, Tehran, Iran, in 2001, 2004 and 2014, respectively. His current research interests include wavelet Galerkin method, finite element method, and biomedical instrumentation.

**Farouk Smith** received the bachelor of science degree in physics (1994), the bachelor of science in electronics engineering (1996), and the master of science in electronics engineering at University of Cape Town (2003). He received the Ph.D. in electronic engineering at the University of Stellenbosch, South Africa, in 2007. He is currently a head of the Department of Mechatronics at Nelson Mandela University. Prof. Smith is also a registered professional engineer with the Engineering Council of South Africa (ECSA) and a Senior Member of the IEEE.

**Shahrokh Hatefi** received his B.Sc. degree in electrical engineering, and the M.Sc. degree in mechatronics engineering from Islamic Azad University, Isfahan, Iran. He was an academic lecturer in Islamic Azad University in Iran from 2014 to 2016. He worked as a mechatronics specialist in Isfahan Steam Enterprise from 2016 to 2017. He is currently a part-time faculty member and lecturer in Nelson Mandela University. In 2015, he produced a patent on a medical device "Digital Absolang". He also published articles in the fields of precision engineering and biomedical engineering. He is interested in research on different fields of mechatronics engineering and multidisciplinary applications. Mr. Hatefi is currently a member of Precision Engineering Laboratory of Nelson Mandela University where he is busy with his Ph.D. degree on hybrid precision machining technologies.

**Khaled Abou-El-Hossein** has obtained his M.Sc. degree in engineering and Ph.D. degree from National Technical University of Ukraine in the areas of machine building technology and advanced manufacturing. He is currently a full professor at the Nelson Mandela University in South Africa. During his academic career, he occupied a number of administration positions. He was the Head of mechanical engineering Department in Curtin University (Malaysia). He was also the Head of Mechatronics Engineering and Director of School of Engineering in Nelson Mandela University. He published extensively in the areas of machining technologies and manufacturing of optical elements using ultra-high precision diamond turning technology. Prof. Abou-El-Hossein is registered researcher in the National Research Foundation of South Africa (NRF SA). He is also a registered professional engineer in the Engineering Council of South Africa (ECSA).

**Jason Z. Kang** received his Ph.D. degree in 1988 from University of Electronic Science and Technology of China (UESTC), Chengdu, China. He was a research fellow at University of Birmingham and Loughborough University, UK in 1990~1992. Since 1984 he has been with UESTC. Currently he is a full professor with Chengdu College of UESTC. Dr. Kang published more than 80 papers and book chapters, named Jason Z. Kang, Zhusheng Kang, Zhu-Sheng Kang, and his Chinese name. His research interests include electronic systems, power electronics, energy efficient architectures, clean energy, and etc. Prof. Kang was invited to have short-term academic visits to American University of Sharjah, UAE in 2014, Offenburg University of Applied Sciences, Germany in 2015, and Universiti Tunku Abdul Rahman, Malaysia in 2013 and 2018. Together with Prof. Danny Sutanto, University of Wollongong, Australia, he initiated International Conference on Smart Grid and Clean Energy Technologies (ICSGCE) in 2010 and has always been the steering Organizing Chair of ICSGCE. Prof. Kang is an active editors of several publications, including executive editor-in-chief and editor-in-chief of Journal of Electronic Science and Technology in 2007~2017, executive editor-in-chief of Journal of Communications since 2010, and executive editor-in-chief of International Journal of Electrical and Electronic Engineering & Telecommunication since 2018.